



Construction of p-n heterojunction β -Bi₂O₃/BiVO₄ nanocomposite with improved photoinduced charge transfer property and enhanced activity in degradation of *ortho*-dichlorobenzene

Juanjuan Sun^a, Xinyong Li^{a,c,*}, Qidong Zhao^b, Moses O. Tadé^c, Shaomin Liu^c

^a State Key Laboratory of Fine Chemicals, Key Laboratory of Industrial Ecology and Environmental Engineering MOE, School of Environmental Science and Technology, Dalian University of Technology, Dalian 116024, China

^b School of Petroleum and Chemical Engineering, Dalian University of Technology, Panjin Campus, Panjin 124221, China

^c Department of Chemical Engineering, Curtin University of Technology, Perth, WA 6845, Australia



ARTICLE INFO

Article history:

Received 17 March 2017

Received in revised form 13 July 2017

Accepted 19 July 2017

Available online 22 July 2017

Keywords:

Nanostructured photocatalysts

Photo-induced charge carriers

p-n Heterojunction

In situ FTIR

ortho-Dichlorobenzene

ABSTRACT

To achieve efficient conversion of solar to chemical energy in photocatalysis, development of visible-light-induced catalysts with high charge carrier mobility and superior activity is essential. In this work, a novel β -Bi₂O₃/BiVO₄ nanocomposite with p-n heterojunction structure, which is assembled by interconnected quantum dots, has been successfully constructed through a facile approach. The structural and optical properties of the as-prepared materials were comparatively characterized. Steady-state and transient-state photoluminescence spectra demonstrate that the photo-induced charge carriers in β -Bi₂O₃/BiVO₄ nanocomposite display higher separation and much longer lifetime than those in individual BiVO₄ samples, which is attributed to the formation of efficient interfacial electric field between β -Bi₂O₃ and BiVO₄. The photocatalytic performance of the samples was explored by the degradation of *ortho*-dichlorobenzene (*o*-DCB). Electron spin resonance examinations confirmed that much more superoxide radicals were generated in the system of β -Bi₂O₃/BiVO₄ nanocomposite, which could be mainly responsible for the outstanding activity. In addition, the adsorption and oxidation of *o*-DCB over the as-prepared materials were studied by *in situ* FTIR spectroscopy to investigate the nature of surface intermediates formed on the catalysts. To clarify charge migration route, a detailed photocatalytic mechanism in terms of the energy band structures is proposed.

© 2017 Elsevier B.V. All rights reserved.

1. Introduction

Since the discovery of photolysis water on TiO₂ electrodes under ultraviolet irradiation by Fujishima and Honda in 1972 [1], photocatalysis as an efficient, green and promising technology, has gained extensive attention for several decades. Particularly, the semiconductor-based photocatalysts with advanced nanostructures, which possess favorable charge transport properties and huge surface to volume ratios, holds great potential in the fields of solar-to-chemical energy conversion and environmental purification [2,3]. As well known, the high utilization of solar energy, bulk diffusion of photo-excited charges and the charge kinetics which include the three curial steps, *i.e.* the generation, separation, and

consumption, play the key role in the process of photocatalysis [4–6]. To improve the photocatalytic activity, many efforts based on the above fundamental factors have been made to design and develop new, highly efficient photocatalysts [7–9]. Additionally, reducing the particle size could be beneficial to the charge carriers transfer from bulk to surface and increase of the specific surface area that closely associated with reactive sites. Owing to the favorable carriers mobility and new physical properties, nanostructured materials have attracted extensive attention and been widely used for energy-related applications [3,10,11].

Among the emerging catalysts, scheelite-monoclinic *n*-type semiconductor BiVO₄ (*m*-BiVO₄) has attracted significant and continuously attention as a promising material for oxygen evolution from water splitting [12–14] and environmental rehabilitation [15–17], because of the narrow band gap (~2.4 eV), favorably positioned band edges and higher photo-activity in comparison with its crystal-structure counterparts [18]. However, the poor carrier separation and mobility properties are the intrinsic drawbacks of *m*-BiVO₄. Hence, lots of efforts have been afforded

* Corresponding author at: State Key Laboratory of Fine Chemicals, Key Laboratory of Industrial Ecology and Environmental Engineering MOE, School of Environmental Science and Technology, Dalian University of Technology, Dalian 116024, China.

E-mail addresses: xyli@dlut.edu.cn, xinyongli@hotmail.com (X. Li).

to address the shortcomings by modifying electronic structure, constructing favorable surface structure with heterojunction or controlling morphologies [19–21]. In particular, the fabricated heterojunction of the p-type and n-type semiconductors with suitable relative band edge positions can facilitate interfacial charge transfer and increase the lifetime of the carriers in a solar energy conversion system. Recently, a kind of p-type Bi_2O_3 semiconductor as the simplest bismuth oxides has drawn considerable attention due to the multiple properties, such as multifold crystallographic polymorphs (α -, β -, γ -, δ , and ε -), wide band-gap range (2.0–3.96 eV), good electrochemical performances and high oxygen-ion conductivity [22,23]. Among the five different polymorphs, the tetragonal β - Bi_2O_3 shows excellent photocatalytic activity owing to the smaller band gap, more dispersive band structures and stronger oxidative ability [24,25].

Herein, we have fabricated the p-n heterojunction material of m - BiVO_4 modified by β - Bi_2O_3 with small-dimension nanostructure to utilize visible light effectively and facilitate the separation and transfer of photoexcited charge carriers. In this work, the β - $\text{Bi}_2\text{O}_3/\text{BiVO}_4$ nanocomposite assembled by quantum dots, has been constructed by a facile one-pot hydrothermal method, and is utilized for the degradation of gaseous *ortho*-dichlorobenzene (*o*-DCB) under visible-light irradiation. The novel β - $\text{Bi}_2\text{O}_3/\text{BiVO}_4$ nanocomposite exhibited much higher activity than the individual BiVO_4 samples and the similar state-of-the-art material Q- $\text{BiVO}_4/\text{TiO}_2$ [26], because of the prolonged charge carriers lifetime and effective generation of reactive oxide species. Additionally, the crystal structure, morphologies and optical properties of the as-prepared catalysts were comparatively characterized. The degradation intermediates of *o*-DCB in photocatalytic process over the BiVO_4 -based catalysts are identified by *in situ* FTIR for the first time. Besides, the mechanism of photoinduced charge transfer in the β - $\text{Bi}_2\text{O}_3/\text{BiVO}_4$ nanocomposite is proposed in terms of the energy band structures.

2. Experimental section

2.1. Materials

All chemical reagents which were purchased from Sinopharm Chemical Reagents Co., Ltd., China, were analytical grade and used without further purification.

2.2. Synthesis of β - $\text{Bi}_2\text{O}_3/\text{BiVO}_4$ nanocomposite

In a typical synthesis, 2.2 mmol sodium oleate was put into 20 mL distilled water, and then 0.6 mmol $\text{Bi}(\text{NO}_3)_3 \cdot 5\text{H}_2\text{O}$ was added to the dispersion of sodium oleate with magnetic stirring for ca. 20 min. Then, an aqueous solution (20 mL) containing $\text{Na}_3\text{VO}_4 \cdot 2\text{H}_2\text{O}$ (0.4 mmol) was dropped into the above solution. After vigorous stirring for 120 min, the mixture was transferred to a 50 mL Teflon-lined autoclave, sealed and heated at 150 °C for 18 h. The system was then allowed to cool to room temperature naturally. The sample was collected by centrifugation and washed with *n*-hexane and absolute ethanol several times. Finally, the obtained products was dried at room temperature under vacuum for further characterization.

2.3. Synthesis of BiVO_4 nanocrystal

In a typical preparation, 4 mmol $\text{Bi}(\text{NO}_3)_3 \cdot 5\text{H}_2\text{O}$ and 4 mmol NH_4VO_3 were successively added to 100 mL distilled water. And then 1 g polyethylene glycol 20000 as surfactant, was put into the above solution with stirring. The pH value of the obtained microemulsion was gradually adjusted to about 7 by dilute ammonia solution. Subsequently, the mixture was stirred intensely for 1 h at room temperature, and then was exposed to high-intensity

ultrasonic irradiation in ambient air. The yellow precipitates were collected by centrifugation, washed with de-ionized water and absolute ethanol repeatedly, and dried at 60 °C overnight. The obtained sample was calcined in a muffle furnace at 450 °C for 2 h at a ramp rate of 1 °C/min.

2.4. Synthesis of BiVO_4 ellipsoid

In a typical synthesis, 2 mmol of $\text{Bi}(\text{NO}_3)_3 \cdot 5\text{H}_2\text{O}$ was put into 60 mL ethylene glycol, and 2 mmol of NH_4VO_3 was dissolved in 20 mL de-ionized water to form the solution. Subsequently, the solution was dropped into the dispersion containing $\text{Bi}(\text{NO}_3)_3 \cdot 5\text{H}_2\text{O}$ under intense stirring. The pH value was adjusted to 5.0 with diluted hydrochloric acid. After stirring for about 60 min, the mixture was transferred into a 100 mL Teflon-lined autoclave, sealed and heated at 150 °C for 16 h. Afterward, the system was allowed to cool down to room temperature naturally. The product was collected by centrifugation, washed with de-ionized water and absolute ethanol repeatedly, and finally dried overnight for further used.

2.5. Photocatalyst characterization

The crystalline phase of the as-prepared materials was examined by powder X-ray diffraction (XRD) using a Rigaku D/Max 2550VB/PC diffractometer with a $\text{Cu K}\alpha$ radiation source, an operating voltage of 40 kV and an emission current of 30 mA. The morphologies and microstructures were characterized by a field emission scanning electron microscope (FE-SEM, JEOL JSM-6360LV) and transmission electron microscopy (TEM, JEOL JEM-2000 EX). The high-resolution transmission electron microscopy (HRTEM) was performed on an FEI Tecnai G2 F30 microscope with an acceleration voltage of 300 kV, and was analyzed by the digital Micrograph software. X-ray photoelectron spectroscopy (XPS) measurements were conducted on a Perkin-Elmer PHI 5600 electron spectrometer with $\text{Al K}\alpha$ radiation at 1486.6 eV under ultrahigh vacuum condition. All of the binding energies were calibrated by the surface adventitious carbon (C 1s) at 284.6 eV used as the reference. The special surface area and pore size were determined through nitrogen sorption experiments at 77.3 K using an automated adsorption analyzer (Quadasorb-SI) by the multipoint method. The UV-vis diffuse reflectance spectra (DRS) were obtained on an UV-vis spectrophotometer (JASCO, UV-550) with BaSO_4 as the standard sample. The photoluminescence (PL) properties of the samples were examined on a Hitachi F-4500 fluorescence spectrophotometer at room temperature (excited at $\lambda = 325$ nm). The time-resolved PL spectra decay curves were obtained by using a FLSP-920 Edinburgh instrument with 450 W xenon lamp monochromatized by double grating at room temperature. The electron spin resonance (ESR) signals of radicals trapped by 5,5'-dimethyl-1-pirroline-N-oxide (DMPO) (received from Sigma-Aldrich Chemical Co.) were detected on Bruker ECS106 X-Band spectrometer. The visible-light irradiation source was a Phillips 500 W high-pressure xenon arc lamp with a UV-cutoff filter ($\lambda > 400$ nm). In the ESR measurements, identical quartz capillary tubes were used to minimize experimental errors.

2.6. In situ FTIR studies and photocatalytic activity evaluation

Photocatalytic activities of the as-synthesized samples were evaluated by the degradation of gaseous *o*-DCB under visible-light illumination ($\lambda > 400$ nm) in a home-made reaction apparatus which is a quartz cell about 160 mL, equipped with two KBr windows and a sample holder (diameter, 13 mm) for putting the catalyst wafer (20 mg). The reaction atmosphere was air whose relative humidity was 45%. After the wafer was placed in the

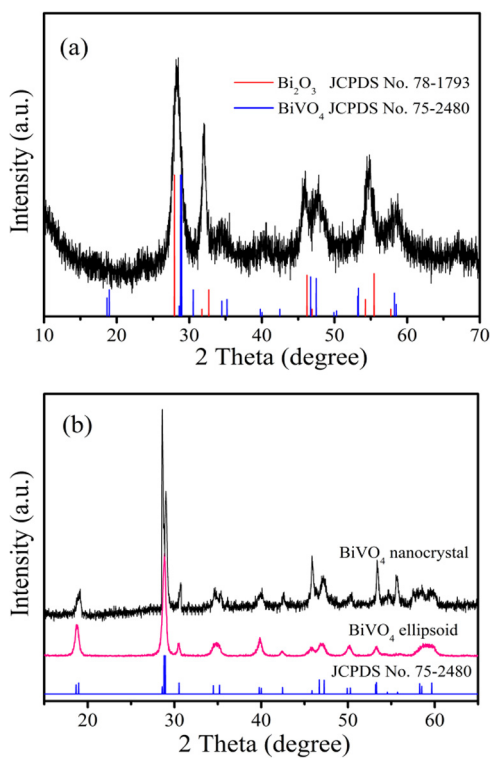


Fig. 1. XRD patterns of the (a) β - Bi_2O_3 /BiVO₄ nanocomposite, (b) BiVO₄ nanocrystal and BiVO₄ ellipsoid.

sample holder kept in the middle of the cell, a small quantity of *o*-DCB (3 μL) was injected into the reaction equipment which subsequently was sealed up. After about two hours in the dark, the fully volatilized *o*-DCB reached adsorption equilibrium, Then, the Xenon lamp (XQ-500W) with a 400 nm UV-cutoff filter was turned on. *In situ* FTIR spectra of reactant on catalysts in the photocatalytic reaction process were obtained using a FTIR spectrometer (Bruker VERTEX 70-FTIR). All of the FTIR spectra were recorded over accumulative 64 scans at a resolution of 4 cm^{-1} in the range of 600 – 4000 cm^{-1} . The concentrations of *o*-DCB in the reaction process were detected by gas chromatogram (Agilent 7890A) equipped with FID (HP-5 capillary column) and TCD (Porapak Q).

3. Results and discussion

Fig. 1 displays the XRD patterns of as-prepared β - Bi_2O_3 /BiVO₄ nanocomposite, BiVO₄ nanocrystal and BiVO₄ ellipsoid. In Fig. 1a, it can be seen that there are two different XRD patterns in the nanocomposite, which correspond to tetragonal β - Bi_2O_3 (JCPDS No. 78-1793) and *m*-BiVO₄ (JCPDS No. 75-2480) respectively. The diffraction peaks at 2θ of 27.95° , 32.65° , 46.21° , 54.25° and 55.21° could be indexed to the (201), (220), (222), (203) and (421) crystal planes of tetragonal β - Bi_2O_3 , respectively. The peaks around 2θ of 28.79° , 34.49° , 35.19° , 46.05° , 47.27° and 58.26° could be indexed to the characteristic peaks (-112), (200), (020), (123), (024) and (-312) of *m*-BiVO₄, respectively. Besides, the broad nature of the XRD peaks indicates the presence of the small-sized particles. In Fig. 1b, it can be seen that the as-prepared pure BiVO₄ samples are in good agreement with the *m*-BiVO₄ (JCPDS No. 75-2480), and the diffraction peaks are sharp and intense, which indicate the catalysts are highly crystalline.

Fig. 2 illustrates the typical TEM, HRTEM and SEM images of the as-synthesized β - Bi_2O_3 /BiVO₄ nanocomposite and BiVO₄ samples, respectively. Fig. S1 shows the morphology of β - Bi_2O_3 /BiVO₄ nanocomposite. Furthermore, in Fig. 2a, it can be seen that the β -

Bi_2O_3 /BiVO₄ nanocomposite appears as nanoparticles with size in the range of 20–50 nm. A TEM image of higher resolution indicates (Fig. 2b) the nanocomposite is composed of interconnected quantum dots with diameter of about 5 nm. [27,28] The composition and microstructure features of the β - Bi_2O_3 /BiVO₄ nanocomposite were further studied by SAED and HRTEM. The corresponding SAED pattern is shown in Fig. 2c. The ring pattern reveals the polycrystalline nature of the formed nanoparticles. Furthermore, the rings are clear and sharp, which suggests that the crystalline grains could be tiny and scatter evenly. The separated diffraction rings of the SAED pattern respectively correspond to (201), (421), (020) and (123) planes of β - Bi_2O_3 and BiVO₄, showing that the nanoparticles are consisted of two crystal forms and the heterojunction microstructure between nanoparticles is formed. This is also supported by the HRTEM image in Fig. 2d. The fast Fourier transform (FFT) pattern and inverse FFT pattern of the selected area marked by the ellipse and rectangle (Fig. 2e-g) further clearly display the crystalline structure of the β - Bi_2O_3 /BiVO₄ nanocomposite. The measured lattice fringes of 0.319, 0.309 and 0.254 nm match well with the inter-plane spacing of the (201) crystallographic planes of β - Bi_2O_3 , (112) and (020) planes of *m*-BiVO₄ respectively. The typical SEM and TEM images of the as-prepared BiVO₄ catalysts are shown in Fig. 2h, i and Fig. S2. In Fig. 2h, it can be seen that the average size of the well-separated BiVO₄ nanocrystal is about 100 nm. As shown in Fig. 2i, the morphology of the as-obtained sample is uniform ellipsoid and the length is about 1 μm .

The surface compositions and chemical status of elements of β - Bi_2O_3 /BiVO₄ nanocomposite were analyzed by XPS. Fig. 3 is a typical XPS survey spectrum and high-resolution XPS spectra of Bi 4f, V 2p and O 1s. As shown in Fig. 3a, only the characteristic peaks of Bi, V, O and C elements were detected on the surface of the sample. The observed peak for C 1s around 284.6 eV is attributed to the signal from adventitious carbon in the instrument. The peaks located at 159.0 eV and 164.3 eV can be assigned to the Bi 4f_{5/2} and Bi 4f_{7/2}, respectively, confirming that the bismuth species in the nanocomposite are Bi³⁺ cations (Fig. 3b) [29]. Two bands at 516.8 eV (V 2p_{3/2}) and 524.2 eV (V 2p_{1/2}) are ascribed to the split signal of V 2p (Fig. 3c), suggesting the existence of the V⁵⁺ oxidation state [30]. In Fig. 3d, the asymmetrical O 1s signal is fitted into three bands at 529.6, 530.0 and 531.0 eV. The peaks at 529.6 and 530.0 eV are corresponded to the Bi–O bond of β - Bi_2O_3 and the oxygen species of lattice oxygen (O²⁻) in BiVO₄, respectively. The band at 531.0 eV is attributed to surface adsorbed oxygen species as hydroxyl-like group or O⁻ defect oxide [31,32].

Fig. 4 presents the N₂ adsorption-desorption isotherms (inset) and pore size distribution curves of the obtained samples. The corresponding specific surface area and pore size distribution were respectively determined by the Brunauer–Emmett–Teller (BET) and Barrett–Joyner–Halenda (BJH) method, which are summarized in Table S2. All of the photocatalysts correspond to type IV adsorption-desorption with a H1 hysteresis loop, suggesting the existence of mesoporous structure [33]. Compared with the apparent areas of BiVO₄ ellipsoid and BiVO₄ nanocrystal, the BET surface area of the β - Bi_2O_3 /BiVO₄ nanocomposite was larger, and the pore size distribution was more uniform. The enhancement might be attributed to the small particle size of the nanocomposite. Based on the BET investigation, the β - Bi_2O_3 /BiVO₄ nanocomposite with uniform mesoporous structure possesses the larger surface areas, which could provide more active sites, beneficial to the catalytic activity.

The optical properties of the materials are studied by UV-vis diffusion spectroscopy. As shown in Fig. 5a, in contrast with the pure BiVO₄ samples which exhibit a little stronger absorption in the visible range with a steep absorption edge, β - Bi_2O_3 /BiVO₄ nanocomposite has a nonsteep absorption edge. The nonsteep absorption could be ascribed to its tiny particular morphology [34].

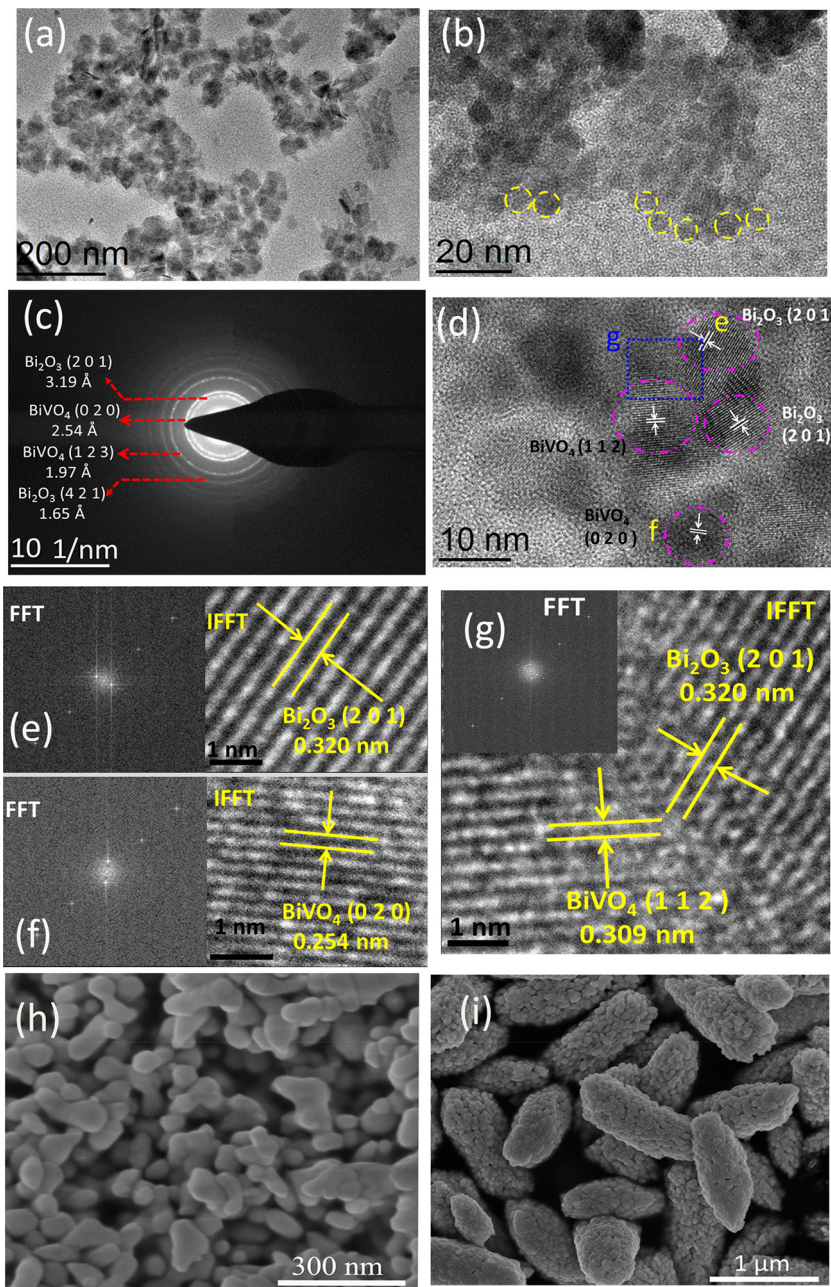


Fig. 2. Typical TEM and SEM images of the as-prepared samples. TEM (a, b), the corresponding SAED pattern (c) and HRTEM (d–g) images of the β - $\text{Bi}_2\text{O}_3/\text{BiVO}_4$ nanocomposite. SEM (h, i) images of BiVO_4 nanocrystal and BiVO_4 ellipsoid.

Furthermore, it is found that the β - $\text{Bi}_2\text{O}_3/\text{BiVO}_4$ nanocomposite exhibited broad background absorbance in the visible region, which may be attributed to surface defect states or the room-temperature exciton absorption in the semiconductor [35,36]. The band-gap energy of the obtained samples can be estimated from the Tauc's plots [37]. Plots of $(\alpha h\nu)^2$ versus $h\nu$ of the samples are presented in Fig. 5b. The intercept of the tangents to the X axis exhibits a good approximation of the band gap energy of the samples. The band gaps of BiVO_4 ellipsoid, BiVO_4 nanocrystal and β - $\text{Bi}_2\text{O}_3/\text{BiVO}_4$ nanocomposite are estimated to be about 2.41, 2.47 and 2.45 eV, respectively, suggesting that the obtained samples do not have the big difference in the ability of light absorption.

PL emission is closely related to the recombination of excited electrons and holes. Herein, the PL characteristics of the as-prepared samples were studied to reveal interfacial charge transfer

dynamics. Generally, the lowering of the emission intensity is indicative of a decrease in the radiative recombination and a high separation efficiency of electron–hole pairs [38,39]. As shown in Fig. 6a, the β - $\text{Bi}_2\text{O}_3/\text{BiVO}_4$ nanocomposite exhibits diminished PL intensity in comparison with pure BiVO_4 nanocrystal and BiVO_4 ellipsoid, suggesting that the existence of the p-n heterojunction results in a remarkable decline in the recombination of electron–hole pairs. Typically, the broad emission peaks appear around 538 nm of the samples may be caused by the surface-states related recombination of the electron–hole pairs. The emission band at 500 nm of BiVO_4 ellipsoid can be attributed to band-edge emission of free excitons. The emergence of the blue-shifted photoluminescence peaks with wavelength around 467 nm revealed the existence of high energy electron–hole pairs in the β - $\text{Bi}_2\text{O}_3/\text{BiVO}_4$ nanocomposite [34,40].

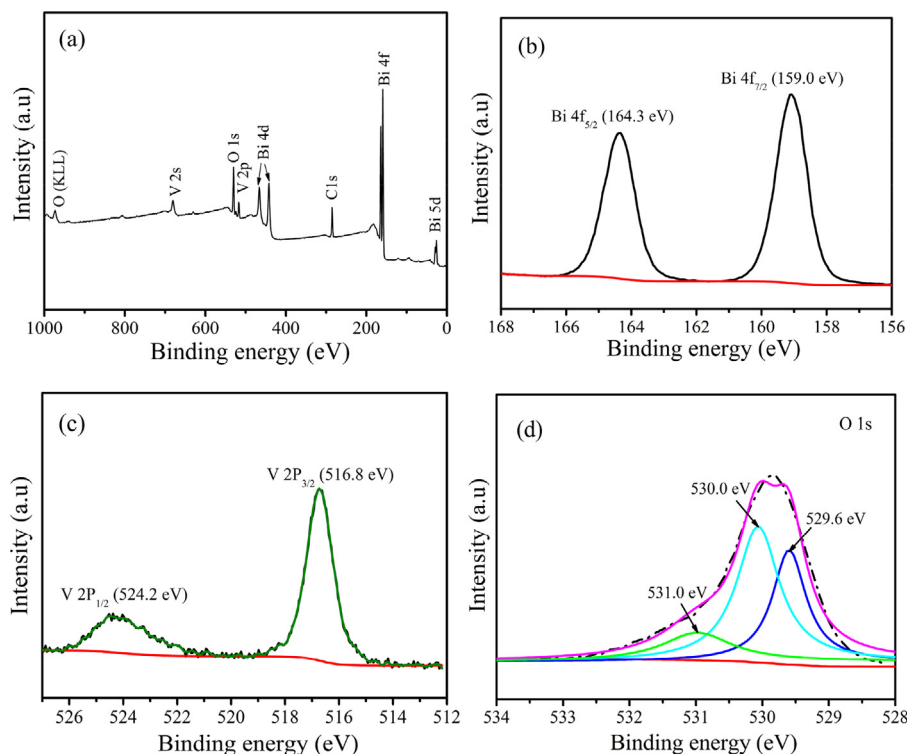


Fig. 3. Survey (a) XPS spectrum, Bi 4f (b) XPS spectrum, V 2p (c) XPS spectrum and O 1s (d) XPS spectrum of β - Bi_2O_3 /BiVO₄ nanocomposite.

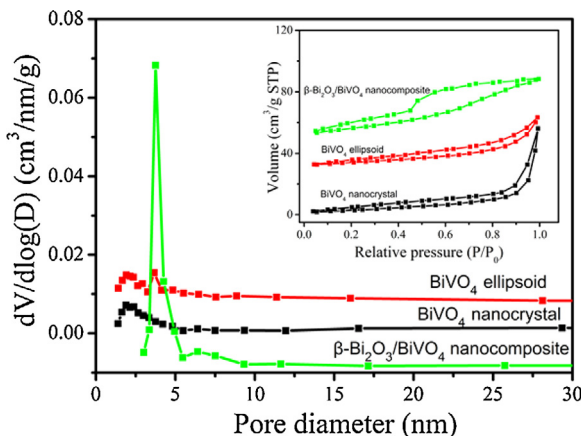


Fig. 4. N_2 adsorption-desorption isotherms (inset) and the corresponding BJH pore distribution curves of the samples.

Time-resolved PL provides important information about the exciton lifetime which represents a crucial indicator of the efficiency of the radiative recombination of the photoinduced charges. The results of measurements are shown in Fig. 6b and summarized in Table S3. From Fig. 6b, it can be seen that the PL peak decay of β - Bi_2O_3 /BiVO₄ nanocomposite was much slower than those of BiVO₄ nanocrystal and BiVO₄ ellipsoid. Additionally, the β - Bi_2O_3 /BiVO₄ nanocomposite exhibited biexponential decay, while BiVO₄ nanocrystal and BiVO₄ ellipsoid exhibited single-exponential decay. The biexponential model of β - Bi_2O_3 /BiVO₄ suggested that two emissive states were involved in the PL decay with $\tau_1 = 0.62$ ns and $\tau_2 = 10.00$ ns. The fast decay constant (τ_1) was typically attributed to the radiative emission of direct interband exciton recombination, while the much slower decay constant (τ_2) was originated from the radiative emission via indirect recombination of trapped electrons with VB holes [41–43]. Direct recombination of excitons was predominated in the pure

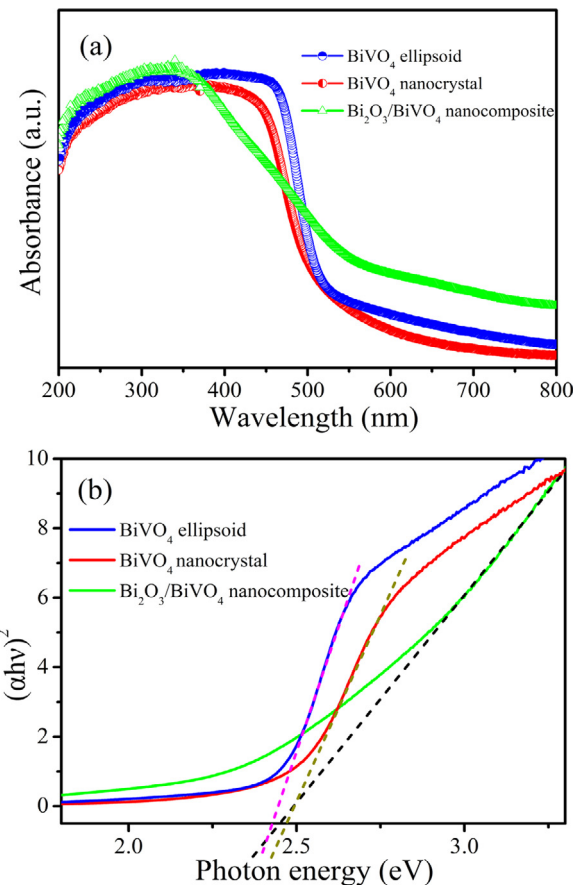


Fig. 5. Optical absorption properties of the as-prepared samples: UV-vis diffuse reflectance spectra (a) and the energy gap calculated by plotting $(\alpha h\nu)^2$ versus $h\nu$ (b).

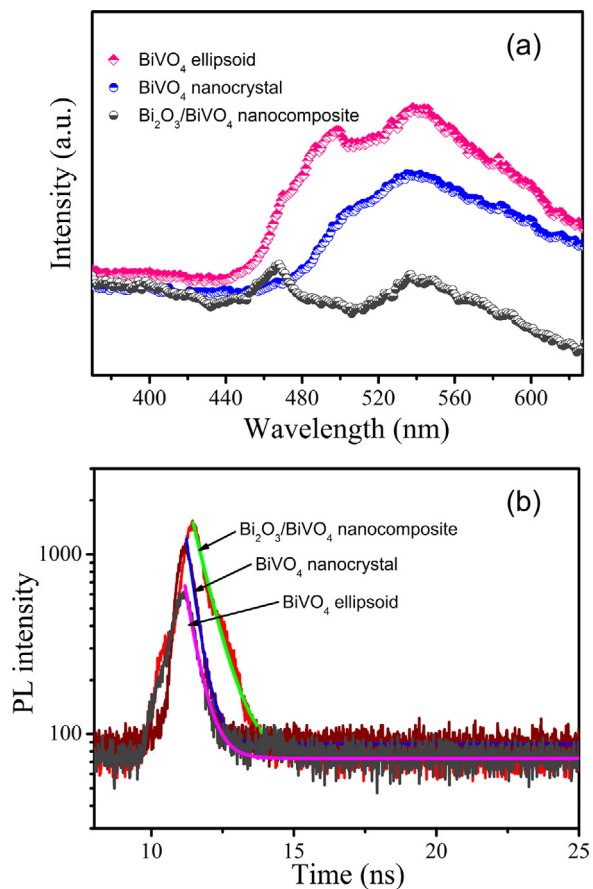


Fig. 6. (a) Room-temperature steady-state PL spectra of the samples. (b) The corresponding time-resolved PL decay curves.

BiVO₄ samples, as revealed by its high proportion of short-living component ($B_1\tau_1$ 100%). As shown in Table S3, the τ_1 value for BiVO₄ nanocrystal is longer than that for BiVO₄ ellipsoid, suggesting a more effective separation of electrons and holes in BiVO₄ nanocrystal. Furthermore, it can be seen that the longer lifetime (τ_2) only exist in the β -Bi₂O₃/BiVO₄ nanocomposite, the τ_1 value of which is the longest among the as-prepared samples. This result indicates that the lifetime of photo-generated charge carriers was prolonged, and an efficient separation and transfer of electron-hole pairs occurred within the β -Bi₂O₃/BiVO₄ nanocomposite [44].

As is known, o-DCB is an important precursor of polychlorinated dibenzodioxins and dibenzofurans which are highly toxic, carcinogenic, and persistent. Due to the structural similarity, o-DCB has been frequently used as the model compound for investigating catalytic oxidation of these complex chlorinated organic compounds [45,46]. In this work, the adsorption and reaction processes of the gaseous o-DCB over the prepared β -Bi₂O₃/BiVO₄ nanocomposite were studied detailedly by *in situ* FTIR spectroscopy. As shown in Fig. 7a, the FTIR spectra were collected at different time intervals during o-DCB adsorption at room temperature. The characteristic absorption bands appearing at 1578, 1460 and 1435 cm⁻¹ can be assigned to the C=C degenerate stretching vibrations of the aromatic ring [46]. The band at 1130 cm⁻¹, so-called substituent-sensitive, has been assigned to the Ar-Cl stretching vibrations, and the band at 1039 cm⁻¹ belongs to ring C-H in-plane bending vibrations [47,48]. The absorption intensity of these characteristic bands of o-DCB reached peak after 90 min and did not show any enhanced tendency at 100 min and 120 min, indicating that the adsorption-desorption process of gaseous o-DCB over the catalyst reached equilibrium.

When the gas-solid regime reached adsorption equilibrium, the system was irradiated with visible light ($\lambda > 400$ nm). As shown in Fig. 7b, the intensities of the bands at 1578, 1460, 1435, 1130, 1039 and 748 cm⁻¹ decreased gradually as irradiation time extended. Among them, the band at 748 cm⁻¹ is assigned to ring C-H out-of-plane bending vibration. It is observed that after 6 h, most of o-DCB was decomposed. Simultaneously, the bands appearing at 2400~2300 cm⁻¹ can be attributed to the formation CO₂ species (Fig. 7c). Besides, a lot of new adsorbed surface species were formed with the photocatalytic reaction proceeding, which can be evidenced by *in-situ* FTIR spectra in Fig. 7e. The band at 1293 cm⁻¹ and the broad shoulder present at 1247 cm⁻¹ are assigned to C=O stretching vibration corresponding to surface phenolate or catechol specie, formed after nucleophilic substitution of chlorine atoms on different sites [49,50]. New bands at 1525 and 1548 cm⁻¹ are attributed to COO⁻ asymmetric stretching vibration of surface carboxylate groups [51]. The new shoulder at 1508 cm⁻¹ belongs to the vibration of surface carbonate [52]. It is clearly observed that the intensity of the band at 1548 cm⁻¹ became strong and then weak as reaction proceeding, and the position shifted to band at 1542 cm⁻¹, which is assigned to ν_{as} (COO⁻) of acetate [49,53]. A small shoulder band at 1559 cm⁻¹ occurred after 3 h, attributed to the COO⁻ stretching vibrations of surface acetates [50]. Besides, new bands appearing at 1384 and 1339 cm⁻¹ can be assigned to surface carboxylates of the bidentate format [54]. The bands at 1640 and 1630 cm⁻¹ related to the scissor vibration modes of adsorbed water, which disappeared after reaction for 3 h, indicating that it could be oxidized by the photo-induced holes to form the activated oxygen species. New band at 1733 cm⁻¹ was attributed to C=O stretching vibration of the aldehydes, and the band at 1718 cm⁻¹ was assigned to stretching vibration of the carboxylate group COO⁻ of saturated aliphatic acids [52,54]. The band at 1655 cm⁻¹ was related to surface o-benzoquinone-type species derived from further oxidation of surface catechol species, and the ring of which can cleave through electrophilic substitution with bond-breaking, partially oxidized into the surface species such as formates, acetates and carboxylates of saturated aliphatic acids type. Ultimately, these surface species can be mineralized into CO₂, H₂O and HCl, partially. By referring to the above analysis, a possible mechanism for the o-DCB photocatalytic degradation was proposed, as shown in Fig. S4. In addition, Fig. 7f more clearly describes the concentration changes of the intermediate species with time. In Fig. 7d, the bands in the 3750–3600 cm⁻¹ range are ascribed to the vibration of surface hydroxyl groups which play different roles in the photocatalytic process. The surface hydroxyls with bands at 3696, 3684 and 3648 cm⁻¹ are assigned to bridged-OH, acting as adsorption sites of o-DCB. The bands at 3630 and 3615 cm⁻¹ are attributed to water species absorbed on the surface, indicating the formation of water in the reaction process. Besides, the bands at 3735 and 3726 cm⁻¹ are assigned to terminal hydroxyls, which can trap photo-generated holes to form the •OH radical, acting as a source of •OH radicals. [55,56]

Photocatalytic degradation of gaseous o-DCB was selected as a model reaction to investigate the catalytic activity of the as-prepared samples upon visible light excitation (Fig. 8a). As a comparison, a blank experiment (no catalyst) was performed, and it can be seen that o-DCB has been difficult to degrade in direct exposure to visible light. Whereas, for BiVO₄ ellipsoid and BiVO₄ nanocrystal, the degradation ratio of o-DCB reaches about 46% and 52% after 6 h of visible-light irradiation, respectively. Furthermore, it can be observed that the degradation efficiency of o-DCB over the two catalysts is higher in the first three hours than that in the following hours, which may be ascribed to the accumulation of intermediates on the surface, resulting in the gradual inactivation of the catalysts. In addition, for the β -Bi₂O₃/BiVO₄ nanocomposite, the conversion of o-DCB is about 70%. Compared with the single-

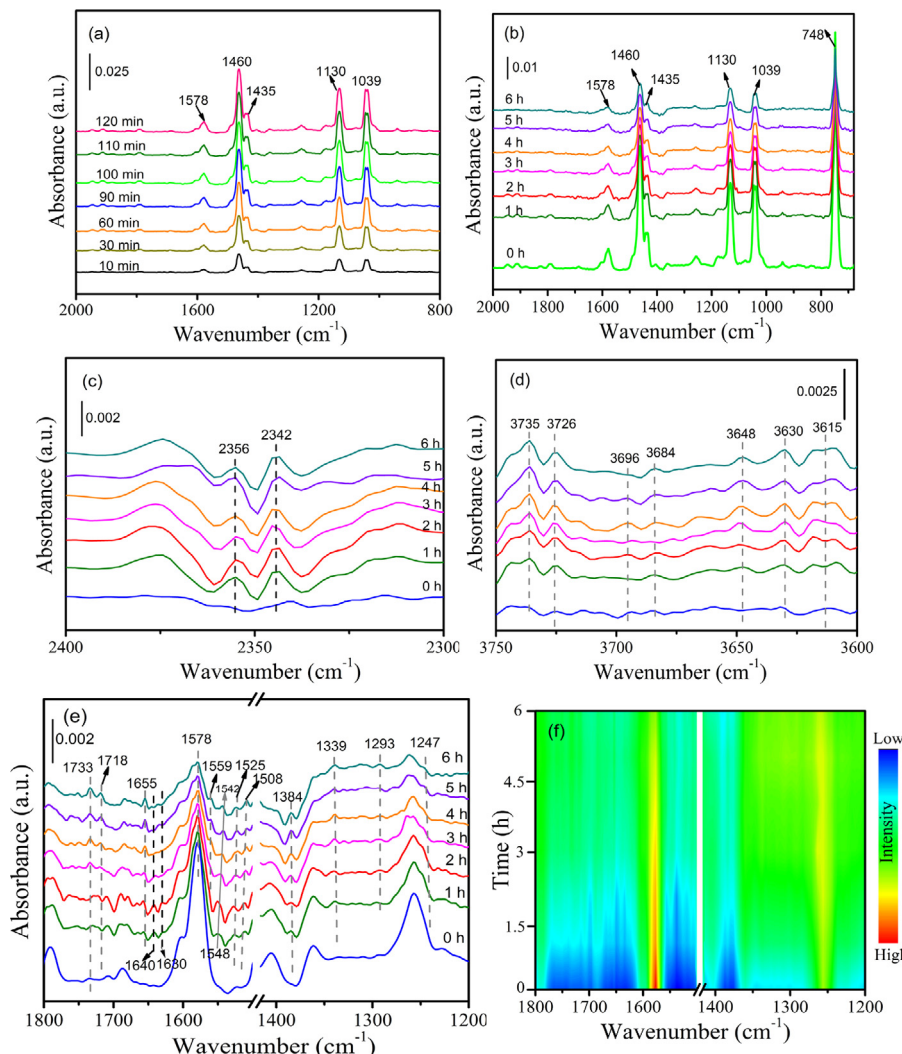


Fig. 7. (a) FTIR spectra of o-DCB absorption on the $\beta\text{-Bi}_2\text{O}_3/\text{BiVO}_4$ nanocomposite. (b–e) *In situ* FTIR spectra of o-DCB photo-oxidation over the $\beta\text{-Bi}_2\text{O}_3/\text{BiVO}_4$ nanocomposite collected at different times under the visible-light irradiation. (f) The corresponding color map recorded in the range of 1800–1200 cm^{-1} .

component samples, the previous researches by our group [53,57], BiVO_4 quantum tubes and the material with similar state-of-the-art heterogeneous structure (Q- $\text{BiVO}_4/\text{TiO}_2$) which is presented in Fig. S6, $\beta\text{-Bi}_2\text{O}_3/\text{BiVO}_4$ nanocomposite displays higher photocatalytic performance, mainly due to the special nanostructure with heterojunction, the superior photo-induced charge separation and long carrier lifetime. The kinetics of photocatalytic degradation of o-DCB over the tested catalysts follows a pseudo-first-order rate law, and the first-order kinetic constants are summarized in Fig. 8b. As shown in Fig. 8b, the apparent rate constant ($2.26 \times 10^{-1} \text{ h}^{-1}$) over the $\beta\text{-Bi}_2\text{O}_3/\text{BiVO}_4$ nanocomposite was about 1.88 and 1.52 times of that over BiVO_4 ellipsoid and BiVO_4 nanocrystal. It is confirmed that the photocatalytic degradation ability for o-DCB over $\beta\text{-Bi}_2\text{O}_3/\text{BiVO}_4$ nanocomposite is higher than that of the individual BiVO_4 samples.

In situ FTIR spectra of o-DCB adsorption on BiVO_4 nanocrystal and BiVO_4 ellipsoid are displayed in Fig. S3. To investigate o-DCB reaction process occurring at the surface of the BiVO_4 nanocrystal and BiVO_4 ellipsoid, typical FTIR spectra of the intermediates in the 1800–1200 cm^{-1} region were studied. From Fig. 9, it can be noticed that the most intermediates are the same as that are found in the photo-oxidation process of o-DCB over the $\beta\text{-Bi}_2\text{O}_3/\text{BiVO}_4$ nanocomposite, suggesting the similar reaction routes. However, the obvious increase in the intensity of the intermediates occurred,

especially with the bands at 1339, 1508, 1548 and 1750 cm^{-1} which are corresponding to surface carboxylate groups. It has been reported that the partially oxidized intermediates (such as carboxylate or carboxylic acid) accumulation on the surface of the catalyst can occupy the active sites, leading to the deactivation of the catalyst, which is consistent with the corresponding photo-degradation results [49,58–60]. The bands at 1640 and 1630 cm^{-1} corresponding to water species also increased, suggesting that they could not be effectively utilized in the reaction.

Due to owning high reaction activity, the reactive oxygen species (ROS) are usually considered to play the key role in the degradation of many environmental organic pollutants. Furthermore, the photocatalytic efficiency as well as the number of photogenerated species are strongly depended on the particle size. Herein, the ESR-spin-trap technique (with DMPO as a trapping reagent) was employed to detect the ROS generated in the as-prepared catalysts during the photocatalytic process, the corresponding ESR spectra are displayed in Fig. 10 and Fig. S5. In Fig. 10a, the typical four peaks of DMPO-•OH adduct were all observed in aqueous dispersions of $\beta\text{-Bi}_2\text{O}_3/\text{BiVO}_4$ nanocomposite, BiVO_4 ellipsoid and BiVO_4 nanocrystal. The intensity of DMPO-•OH for $\beta\text{-Bi}_2\text{O}_3/\text{BiVO}_4$ nanocomposite is almost the same as that for BiVO_4 nanocrystal, while little stronger than that in the suspensions of BiVO_4 ellipsoid.

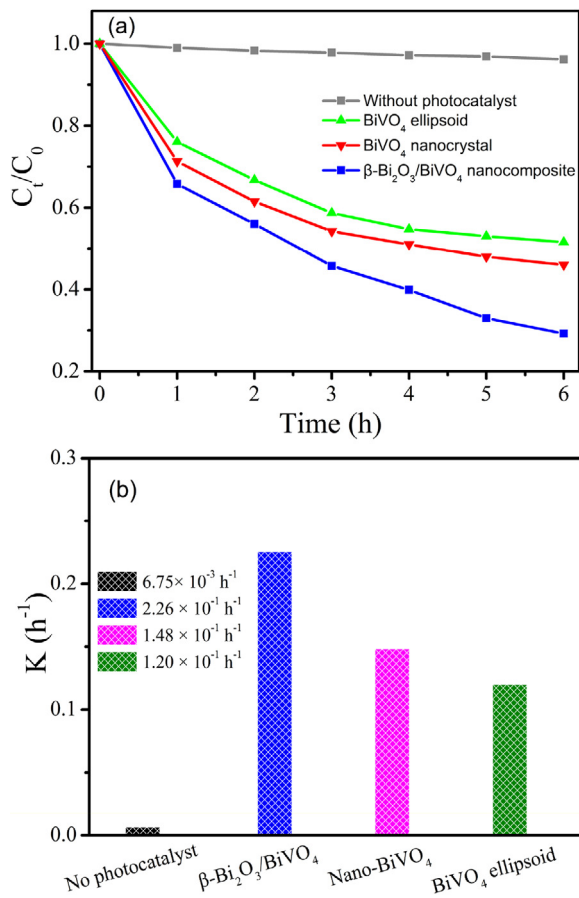


Fig. 8. Comparison of photocatalytic degradation of *o*-DCB (a) and pseudo-first-order kinetic constants (b) over the samples under visible-light irradiation.

In Fig. 10b, the characteristic sextet ESR signal observed is attributed to DMPO-•O₂⁻ adducts. It can be seen that the intensity of DMPO-•O₂⁻ adduct for β -Bi₂O₃/BiVO₄ nanocomposite was much stronger than that for pure BiVO₄, implying that the microstructure of β -Bi₂O₃/BiVO₄ nanocomposite is beneficial for the generation and transfer of the photoelectrons which can be captured by molecular oxygen and lattice oxygen to form •O₂⁻ radical. In addition, the inset of Fig. 10b is the comparison of different ESR signal for β -Bi₂O₃/BiVO₄ nanocomposite. It is observed that the intensity of DMPO-•O₂⁻ adduct is significantly stronger than that of DMPO-•OH adduct, indicating that superoxide radical acts as the predominant species for the oxidation degradation of *o*-DCB. ESR results confirmed that such active oxygen species (•OH and •O₂⁻) were produced in the suspension of β -Bi₂O₃/BiVO₄ nanocomposite under visible light irradiation, and especially superoxide radical was much more generated, mainly responsible for the pretty high photocatalytic activity of β -Bi₂O₃/BiVO₄ nanocomposite. Furthermore, the part of size effect of the catalysts on the photocatalytic efficiency from the heterojunction was discussed in this work. As shown in Fig. S5, the photogenerated ROS was explored in the β -Bi₂O₃/BiVO₄ nanocomposite and BiVO₄ quantum tubes [26] which has similar performance with the quantum dots. Their photocatalytic performance was studied in Fig. S6.

To explain the enhanced photocatalytic activity of β -Bi₂O₃/BiVO₄ nanocomposite, a possible electron-hole pairs separation and transfer mechanism has been proposed in Scheme 1. In accordance with the previous reports, the conduction band (CB) and valence band (VB) edge potentials of p-type β -Bi₂O₃ are approximately 0.29 and 2.67 V versus NHE, respectively [23,61], and those of the n-type BiVO₄ are approximately 0.31 and 2.77 V versus NHE

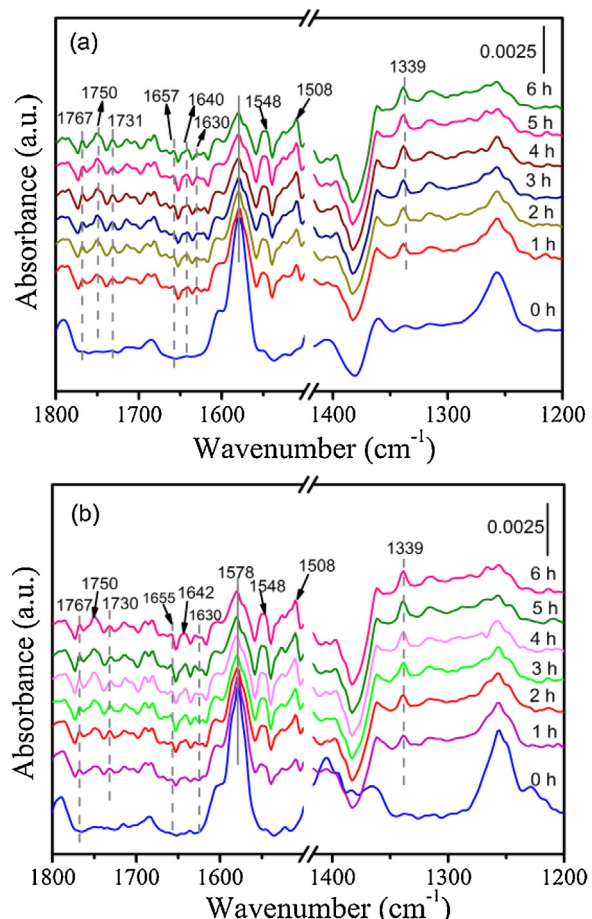


Fig. 9. *In situ* FTIR spectra in the 1800–1200 cm⁻¹ region of *o*-DCB photo-oxidation over the BiVO₄ nanocrystal (a) and BiVO₄ ellipsoid (b).

[29,62]. However, these band-edge positions of β -Bi₂O₃ and BiVO₄ were their potentials before contact. When β -Bi₂O₃ and BiVO₄ were in contact, a p-n heterojunction is formed at the interfacial phase. Furthermore, the interfacing of the two semiconductors with different band structures leads to the charge redistribution to balance the Fermi energy (E_f) which could approach consistency under equilibrium conditions. As a consequence, energy band bending occurs in the space charge region, which can lead to the formation of the internal electric field in the direction from the n-type BiVO₄ to p-type β -Bi₂O₃ that conversely facilitates the separation of electrons and holes in the region [4]. When the p-n heterojunction is established in the interfaces between β -Bi₂O₃ and BiVO₄, the relative positions of the CB and VB of BiVO₄ and β -Bi₂O₃ changed along with the change of the Fermi level [3,63,64]. The energy bands of β -Bi₂O₃ will shift upward to the negative potential, while the bands of BiVO₄ will shift downward to the positive potential until E_f achieve consistency, as shown in Scheme 1b.

When the nanocomposite is irradiated under visible light ($\lambda > 400 \text{ nm}$), the photo-excited electrons (e^-) are generated and transfer from VB into CB of BiVO₄ leaving the corresponding holes (h^+) in the VB. Simultaneously, the same process takes place in β -Bi₂O₃. Through charge redistribution, the CB and VB of β -Bi₂O₃ lie above that of BiVO₄. Because of the more negative CB edge potential of β -Bi₂O₃ than that of BiVO₄ and of O₂/•O₂⁻ (-0.33 V/NHE), the photo-induced electrons tend to migrate toward the CB of BiVO₄, which also can be trapped by the absorbed oxygen molecules to produce superoxide radical anions. Furthermore, due to the more positive VB potential of BiVO₄ than the potential of •OH/H₂O (2.38 V/NHE), the photogenerated holes can trap H₂O and OH⁻ and

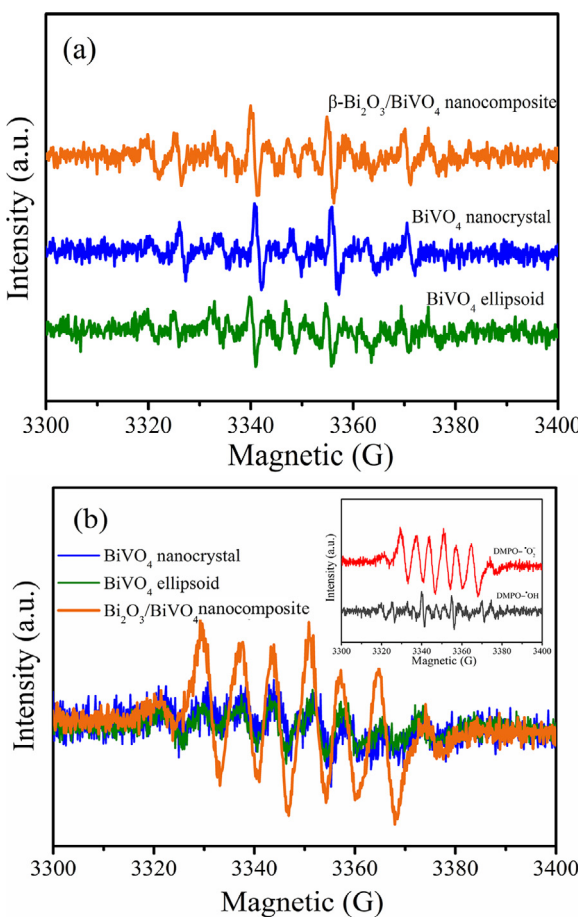
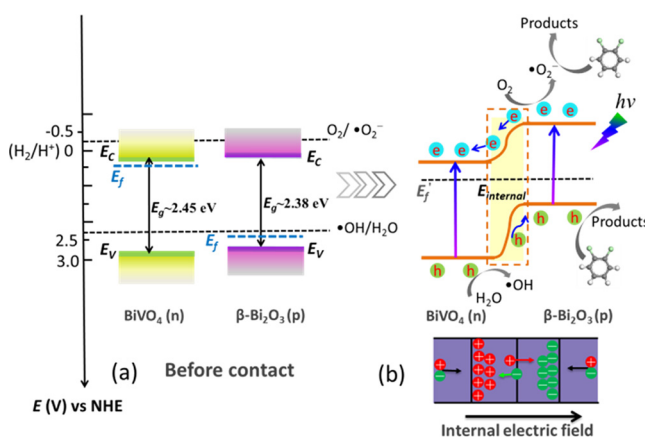


Fig. 10. ESR spectra of DMPO-•OH (a) and DMPO-•O₂⁻ generated with different photocatalysts in aqueous dispersions and methanol dispersions respectively after 240 s visible-light irradiations ($\lambda > 400$ nm). The inset is the comparison of such signal spectra of $\beta\text{-Bi}_2\text{O}_3/\text{BiVO}_4$ nanocomposite.



Scheme 1. Energy band diagram and the possible charge-separation process of $\beta\text{-Bi}_2\text{O}_3/\text{BiVO}_4$ nanocomposite in the case of p-n type contact.

oxidize them to hydroxyl radicals ($\bullet\text{OH}$). However, only a little of the absorbed H_2O and OH^- can be oxidized because most of the holes on the VB of BiVO_4 stream to that of $\beta\text{-Bi}_2\text{O}_3$ and directly oxidize the organic pollutants. Besides, the separation of photo-generated carriers at the interface, followed by further transfer towards different surfaces, can be promoted by the built-in electric field established through p-n heterojunction. The transport of carriers suppress the recombination of electron–hole pairs, extend

the lifetime of the photo-induced charges, and accelerate the photocatalysis reaction process, thus leading to the enhancement of catalytic activity over $\beta\text{-Bi}_2\text{O}_3/\text{BiVO}_4$ nanocomposite.

4. Conclusions

In summary, we have successfully constructed a small-dimension $\beta\text{-Bi}_2\text{O}_3/\text{BiVO}_4$ nanocomposite with an effective p-n heterojunction for improving the photocatalytic performance of BiVO_4 through a facile hydrothermal route. The nanocomposite is innovatively used as an efficient system for degradation of the gaseous o-DCB under visible light irradiation, and the study into the photocatalytic properties proves that the $\beta\text{-Bi}_2\text{O}_3/\text{BiVO}_4$ nanocomposite exhibit much higher activity. The notably enhanced photocatalytic efficiency originates from improved separation for charge transfer and extension of charge lifetime under the effect of interfacial electric field in the elaborately fabricated nanostructure, which ultimately allows the photoinduced electrons and holes to effectively participate in the photocatalytic process. Compared to pure BiVO_4 samples, $\beta\text{-Bi}_2\text{O}_3/\text{BiVO}_4$ nanocomposite can generate much more reactive species ($\bullet\text{O}_2^-$ radicals) which could play a crucial role in the mineralization of o-DCB. Owning to the superior optical properties and high oxidized power, such novel visible-light-harvesting nanocomposite could be a promising alternative for photocatalytic applications.

Acknowledgment

This work was supported financially by the Major Program of the National Natural Science Foundation of China (No. 21590813), the National Natural Science Foundation of China (Nos. 21377015 and 21577012), the Key Project of the National Ministry of Science and Technology (No. 2016YFC0204204), the Program of Introducing Talents of Discipline to Universities (B13012), and the Key Laboratory of Industrial Ecology and Environmental Engineering, China Ministry of Education.

Appendix A. Supplementary data

Supplementary data associated with this article can be found, in the online version, at <http://dx.doi.org/10.1016/j.apcatb.2017.07.052>.

References

- [1] A. Fujishima, K. Honda, *Nature* 238 (1972) 37–38.
- [2] Q. Zhang, E. Uchaker, S.L. Candelaria, G. Cao, *Chem. Soc. Rev.* 42 (2013) 3127–3171.
- [3] H. Tong, S. Ouyang, Y. Bi, N. Umezawa, M. Oshikiri, J. Ye, *Adv. Mater.* 24 (2012) 229–251.
- [4] S. Bai, J. Jiang, Q. Zhang, Y. Xiong, *Chem. Soc. Rev.* 44 (2015) 2893–2939.
- [5] R. Marschall, *Adv. Funct. Mater.* 24 (2014) 2421–2440.
- [6] S. Bai, W. Jiang, Z. Li, Y. Xiong, *ChemNanoMat* 1 (2015) 223–239.
- [7] M. Pelaez, N.T. Nolan, S.C. Pillai, M.K. Seery, P. Falaras, A.G. Kontos, P.S.M. Dunlop, J.W. Hamilton, J.A. Byrne, K. O'Shea, M.H. Entezari, D.D. Dionysiou, *Appl. Catal. B Environ.* 125 (2012) 331–349.
- [8] Y. Qu, X. Duan, *Chem. Soc. Rev.* 42 (2013) 2568–2580.
- [9] X. Gong, Y. Gu, N. Li, H. Zhao, C.J. Jia, Y. Du, *Inorg. Chem.* 55 (2016) 3992–3999.
- [10] A. Hagfeldt, M. Gratzel, *Chem. Rev.* 95 (1995) 49–68.
- [11] A. Kubacka, M. Fernandez-Garcia, G. Colón, *Chem. Rev.* 112 (2012) 1555–1614.
- [12] X. Chang, T. Wang, P. Zhang, J. Zhang, A. Li, J. Gong, *J. Am. Chem. Soc.* 137 (2015) 8356–8359.
- [13] Z. Jiang, Y. Liu, T. Jing, B. Huang, X. Zhang, X. Qin, Y. Dai, M.H. Whangbo, *J. Phys. Chem. C* 120 (2016) 2058–2063.
- [14] S. Hernández, G. Barbero, G. Saracco, A.L. Alexe-Ionescu, *J. Phys. Chem. C* 119 (2015) 9916–9925.
- [15] C. Lv, G. Chen, J. Sun, Y. Zhou, S. Fan, C. Zhang, *Appl. Catal. B Environ.* 179 (2015) 54–60.
- [16] H. Liu, H. Hou, F. Gao, X. Yao, W. Yang, *ACS Appl. Mater. Interfaces* 8 (2016) 1929–1936.
- [17] C. Feng, Z. Jiao, S. Li, Y. Zhang, Y. Bi, *Nanoscale* 7 (2015) 20374–20379.

[18] H. Fan, T. Jiang, H. Li, D. Wang, L. Wang, J. Zhai, D. He, P. Wang, T. Xie, *J. Phys. Chem. C* 116 (2012) 2425–2430.

[19] F.O. Lopes, K.T.G. Carvalho, A.E. Nogueira, W. A Jr., C. Ribeiro, *Appl. Catal. B Environ.* 188 (2016) 87–97.

[20] W. Zhao, Y. Liu, Z. Wei, S. Yang, H. He, C. Sun, *Appl. Catal. B Environ.* 185 (2016) 242–252.

[21] H.J. Kong, D.H. Won, J. Kim, S.I. Woo, *Chem. Mater.* 28 (2016) 1318–1324.

[22] J. Hou, C. Yang, Z. Wang, W. Zhou, S. Jiao, H. Zhu, *Appl. Catal. B Environ.* 142–143 (2013) 504–511.

[23] G. He, C. Xing, X. Xiao, R. Hu, X. Zuo, J. Nan, *Appl. Catal. B Environ.* 170–171 (2015) 1–9.

[24] H. Cheng, B. Huang, J. Lu, Z. Wang, B. Xu, X. Qin, X. Zhang, Y. Dai, *Phys. Chem. Chem. Phys.* 12 (2010) 15468–15475.

[25] F. Zheng, G. Li, Y. Ou, Z. Wang, C. Su, Y. Tong, *Chem. Commun.* 46 (2010) 5021–5023.

[26] J. Sun, X. Li, Q. Zhao, M.O. Tadé, S. Liu, *J. Mater. Chem. A* 3 (2015) 21655–21663.

[27] Y. Sun, Y. Xie, C. Wu, S. Zhang, S. Jiang, *Nano Res.* 3 (2010) 620–631.

[28] J. Hou, Z. Wang, S. Jiao, H. Zhu, *CrystEngComm* 14 (2012) 5923–5928.

[29] Z. He, Y. Shi, C. Gao, L. Wen, J. Chen, S. Song, *J. Phys. Chem. C* 118 (2014) 389–398.

[30] J. Su, X. Zou, G.D. Li, X. Wei, C. Yan, Y.N. Wang, J. Zhao, L.J. Zhou, J.S. Chen, *J. Phys. Chem. C* 115 (2011) 8064–8071.

[31] X. Zhang, L.Z. Zhang, T.F. Xie, D.J. Wang, *J. Phys. Chem. C* 113 (2009) 7371–7378.

[32] X. Ding, K. Zhao, L. Zhang, *Environ. Sci. Technol.* 48 (2014) 5823–5831.

[33] Y. Wang, J. Zhao, T. Wang, Y. Li, X. Li, J. Yin, C. Wang, *J. Catal.* 337 (2016) 293–302.

[34] S. Sun, W. Wang, D. Li, L. Zhang, D. Jiang, *ACS Catal.* 4 (2014) 3498–3503.

[35] D.A.B. Miller, D.S. Chemla, D.J. Eilenberger, P.W. Smith, A.C. Gossard, W.T. Tsang, *Appl. Phys. Lett.* 41 (1982) 679–681.

[36] T.K. Townsend, N.D. Browning, F.E. Osterloh, *ACS Nano* 6 (2012) 7420–7426.

[37] W. Xu, Z. Liu, A.C. Johnston-Peck, S.D. Senanayake, G. Zhou, D. Stacchiola, E.A. Stach, J.A. Rodriguez, *ACS Catal.* 3 (2013) 975–984.

[38] Y. Yu, C.Y. Cao, H. Liu, P. Li, F.F. Wei, Y. Jiang, W. Song, *J. Mater. Chem. A* 2 (2014) 1677–1681.

[39] Q. Huang, S. Tian, D. Zeng, X. Wang, W. Song, Y. Li, W. Xiao, C. Xie, *ACS Catal.* 3 (2013) 1477–1485.

[40] A. Zhu, Q. Zhao, X. Li, Y. Shi, *ACS Appl. Mater. Interfaces* 6 (2014) 671–679.

[41] N.S. Han, H.S. Shim, J.H. Seo, S.Y. Kim, S.M. Park, J.K. Song, *J. Appl. Phys.* 107 (2010) 084306.

[42] M.V. Dozzi, C.D. Andrea, B. Ohtani, G. Valentini, E. Sellì, *J. Phys. Chem. C* 117 (2013) 25586–25595.

[43] Y. Yu, P. Zhang, L. Guo, Z. Chen, Q. Wu, Y. Ding, W. Zheng, Y. Cao, *J. Phys. Chem. C* 118 (2014) 12727–12733.

[44] H. Li, J. Shang, Z. Ai, L. Zhang, *J. Am. Chem. Soc.* 137 (2015) 6393–6399.

[45] H. Duan, J. Li, Y. Liu, N. Yamazaki, W. Jiang, *Environ. Sci. Technol.* 45 (2011) 6322–6328.

[46] J.A. Conesa, L. Rey, S. Egea, M.D. Rey, *Environ. Sci. Technol.* 45 (2011) 5878–5884.

[47] J. Bandara, J.A. Mielczarski, J. Kiwi, *Appl. Catal. B Environ.* 34 (2001) 307–320.

[48] M.A. Larrubia, G. Busca, *Appl. Catal. B Environ.* 39 (2002) 343–352.

[49] B.H. Aristizabal, C. Correa, M.A.I. Serykh, C.E. Hetrick, M.D. Amiridis, *J. Catal.* 258 (2008) 95–102.

[50] T. Cai, H. Huang, W. Deng, Q. Dai, W. Liu, X. Wang, *Appl. Catal. B Environ.* 166–167 (2015) 393–405.

[51] S. Ardizzone, C.L. Bianchi, G. Cappelletti, A. Naldoni, C. Pirola, *Environ. Sci. Technol.* 42 (2008) 6671–6676.

[52] J. Lichtenberger, M.D. Amiridis, *J. Catal.* 223 (2004) 296–308.

[53] B. Liu, X. Li, Q. Zhao, J. Liu, S. Liu, S. Wang, M. Tadé, *J. Mater. Chem. A* 3 (2015) 15163–15170.

[54] X. Ma, Q. Sun, X. Feng, X. He, J. Guo, H. Sun, H. Cao, *Appl. Catal. A* 450 (2013) 143–151.

[55] H. Lin, J. Long, Q. Gu, W. Zhang, R. Ruan, Z. Li, X. Wang, *Phys. Chem. Chem. Phys.* 14 (2012) 9468–9474.

[56] K. Finnie, D. Cassidy, J. Bartlett, J. Woolfrey, *Langmuir* 17 (2001) 816–820.

[57] B. Liu, X. Li, Q. Zhao, J. Ke, M. Tadé, S. Liu, *Appl. Catal. B: Envirion.* 185 (2016) 1–10.

[58] G. Mul, A. Zwijnenburg, B. Linden, M. Makkee, J.A. Moulijn, *J. Catal.* 201 (2001) 128–137.

[59] L. Cao, Z. Gao, S.L. Suib, T.N. Obee, S.O. Hay, J.D. Freihaut, *J. Catal.* 196 (2000) 253–261.

[60] R. Méndez-Román, N. Cardona-Martínez, *Catal. Today* 40 (1998) 353–365.

[61] H. Fan, H. Li, B. Liu, Y. Lu, T. Xie, D. Wang, *ACS Appl. Mater. Interfaces* 4 (2012) 4853–4857.

[62] L. Chen, Q. Zhang, R. Huang, S. Yin, S. Luo, C. T. Au, 41, 2012, 9513–9518.

[63] H. Huang, Y. He, X. Du, P.K. Chu, Y. Zhang, *ACS Sustain. Chem. Eng.* 3 (2015) 3262–3273.

[64] H. Huang, K. Xiao, Y. He, T. Zhang, F. Dong, X. Du, Y. Zhang, *Appl. Catal. B: Environ.* 199 (2016) 75–86.